Fitting Scattering Profiles of Perfluorinated Sulfonic Acid Ionomer Dispersions

E. Jeong[a] and S. Litster[a]

[a] Department of Mechanical Engineering, Carnegie Mellon University, Pittsburgh, Pennsylvania 15213, USA

Polymer electrolyte fuel cells (PEMFCs) are key to developing the hydrogen economy, particularly in the transportation sector. The focus on heavy-duty vehicles has driven research toward improving the efficiency and durability of catalyst layers and understanding the role of the ionomer binder. The characterization of these ionomers is important not only in their cast forms but also in inks and dispersions. Small-angle scattering (SAS) techniques have become one of the primary tools for analyzing ionomer systems in solution. While SAS can provide valuable structural information about ionomer aggregates, relevant size and shape information requires model fitting to obtain. While many scattering form factor models have been applied to uncover the behavior of aggregates in ionomer dispersions, the role of the fitting range in the fit quality has not been extensively discussed. In this work, we illustrate the effect of varying fitting ranges for three commonly used form factors.

Introduction

Perfluorinated sulfonic acid (PFSA) ionomers are an integral material for PEMFCs, not only as an electrolyte membrane but also as a binder for the catalyst layers of the electrodes. In a typical fabrication process, an ink is prepared as a suspension of ionomer, solvent, and catalyst supported on carbon particles, which is then coated as a thin layer onto a substrate to form the catalyst layer (1-2). Once the solvent evaporates, a porous structure of carbon aggregates forms, bound together by the ionomer (1). Thus, the ordering of the polymer chains in the ionomer dispersion during ink processing plays a role in the final catalyst layer structure. Given the vital role of ionomers for proton conductivity and gas transport in the catalyst layer, much work has been devoted to understanding the influence that the processing conditions of the catalyst ink have on the structure of the resulting catalyst layers (2). With recent PEMFC research focusing on heavy-duty vehicles, and targets for efficiency and durability established by the US Department of Energy (3), there is a need to understand the relationship between the processing conditions of ionomers in catalyst inks and the subsequent performance of the catalyst layers.

The structure of ionomer dispersions in different solvent environments has been extensively studied in the literature for conventional ionomers, such as Nafion™. TEM imaging of Nafion™ in solution has shown the polymer chains will form elongated bundles or aggregates (1,4), an idea which has long been supported by small-angle scattering by x-rays (SAXS) or neutrons (SANS) (4-6). SAXS and SANS, extensively used in the literature on ionomer dispersions, can provide information about the order, shape, and size of particles in a solution sample by analyzing the profile of intensity I as a function of the

scattering vector q. The scattering intensity $I(q)$ can be expressed as a product of a form factor $F(q)$ and a structure factor $S(q)$, which represent the shape and size of the scattering particles and the interference due to the ordering of the particles, respectively (6). For ionomer dispersions, the scattering particles are the aggregates of polymer chains, meaning SAXS and SANS can provide information about the form and order of the polymer chains in the dispersion. For instance, the value of q at which the interference peak occurs is often used to indicate a characteristic d-spacing between the aggregates, with the relation $d = 2\pi/q$ (5,7-9).

Inference of the shape of the scattering particle is based on the shape of the intensity profile, particularly at higher values of q where the contribution of $S(q)$ is diminished (6). In the case of a cylindrical particle, a transition from a q^{-1} dependence at intermediate values of q to a q^{-4} dependence at higher q may be seen (4,7,10). Determination of particle sizes involves fitting a known form factor of some geometric model to the scattering data. Among the commonly used form factors are spherical (9,11), infinite-length cylindrical (4,6,7), and finite-length cylindrical models (8,9,11). While the method of fitting form factors can provide size information, the technique is limited when the shape of the scattering particles is unknown, as may be the case for ionomer dispersions at differing concentrations or solvent conditions. Many computational studies have supported the idea of cylindrical, rod-like ionomer aggregates; however, different aggregate shapes have been reported depending on the solvent environment and ionomer concentration. A fully atomistic molecular dynamics study has suggested that the shape of aggregates can vary depending on the polarity of the solvent, with rod-like structures in polar solvents and lamellar structures in solvents of intermediate dielectric constant (12). Other studies have demonstrated a consistent rod-like shape, with changes in the size of the aggregates with ionomer concentration and solvent polarity (13). Despite the differing results for ionomer aggregate shape which have been reported, much of the experimental characterization using SAXS fitting has assumed a cylindrical model. A recent study by Khandavalli et al. found that in dispersions of a PFSA, aggregates were rod-like in low-polarity solvents at low concentrations, and suggested that aggregates may remain rod-like at higher concentrations (9).

In the literature in which form factor fitting is performed, the fit size parameter, typically radius, may be reported as a single value (7) or as a distribution based on a model with polydispersity (8,11). However, the method of selecting a fitting range of q is not often described. The choice of the fitting range can affect the resulting fit parameters and is therefore an important consideration when the specific value of the length parameters is of interest, such as when comparing to TEM results. This dependence of the fit parameter on the fitting range is accounted for in some contexts; for instance, the BioXTAS RAW code performs automated Guinier fitting using an algorithm that searches for a large fitting range with high-quality results by adjusting the criteria for q times the radius of gyration R_g (14). The code also reports an uncertainty, which depends on the variation of the fit R_g over different fitting intervals. In this work, we discuss the effect of choosing a fitting range on the resulting fit values of radius for three form factors: sphere, infinite cylinder, and finite-length cylinder. We investigate the trends in fit quality and the sensitivity of the fit radius to the choice of the start point of the fitting range. Using the experimental data from a concentration series of Nafion dispersion, we investigate how the choice of the fitting range affects the observed trend in radius with concentration. We also share a method to select a

start range that can be automatically applied to scattering data with prominent peaks and does not require manual intervention except for selecting a thresholding parameter.

Methods

Materials and Sample Preparation

We used the commercial Nafion™ D2020 dispersion as the ionomer for this study. Deionized water, 1-propanol, and D2020 were added one by one to a vial and mixed for 10 seconds by a vortex mixer. We prepared five samples at ionomer concentrations of 1%, 3%, 5%, 10%, and 15% by weight at a solvent ratio of 50/50 water to 1-propanol by mass. In addition to the ionomer samples, we prepared reference solvent mixtures at the same 50/50 water to 1-propanol ratio as the dispersions. Each dispersion and reference sample was loaded into a 1.5 mm borosilicate glass capillary using a syringe and polyethylene tubing. The capillaries were sealed using room-temperature-vulcanizing silicone and left to cure for 24 hours before measurement.

SAXS and Data Reduction

SAXS measurements were taken using a Xenocs Xeuss 3.0 instrument with a Rigaku rotating anode Cu source. The Xenocs Instrument Control Center (XICC) software was used to control the Xeuss 3.0, which performs automatic azimuthal averaging of the 2D detector image to a 1D intensity profile with uncertainty values. We used the Xenocs XSACT software to subtract the solvent reference from the ionomer dispersion samples. We present the data on a non-absolute scale due to the difficulty of normalizing to the thickness of the capillaries, which could vary along the length of a single sample, as well as between samples, causing slightly different sample volumes to be measured.

Fitting

We wrote custom code in MATLAB to analyze the subtracted intensity profiles, considering two types of fitting: peak fitting and form factor fitting. For both, the MATLAB 'fit' function was used to perform the optimization. For the peak fitting, we used a Gaussian function; for the form factor fitting, we considered the models for a sphere, infinite cylinder, and cylinder. The form factors for the sphere and finite cylinder are given by Fournet (15) as:

$$I = A\left(3\frac{\sin(qR)-qR\cos(qR)}{q^3R^3}\right)^2 \quad [1]$$

$$I = A\int_0^{\pi/2}\frac{\sin^2\left(\frac{1}{2}qL\cos\theta\right)}{q^2\left(\frac{1}{2}L\right)^2\cos^2\theta}\cdot\frac{4J_1^2(qR\sin\theta)}{q^2R^2\sin^2\theta}\sin\theta d\theta \quad [2]$$

The form factor for the infinite cylinder is given by Porod in Glatter and Kratky's book (16) as:

$$I = A\frac{1}{q}\left(\frac{J_1(qR)}{qR}\right)^2 \quad [3]$$

In the equations above, R represents the radius of the cylinder, L the length, and J_1 the first order Bessel function. Constant terms were collapsed into a scaling factor A. In the case of absolute scattering intensity data, the full expression can provide information about the scattering density or concentration of the samples; however, it is not of interest in this work.

To evaluate the fit quality, reduced χ^2 values were evaluated using the same expression used by the fitting software SasView (17):

$$\chi^2 = \sum_i \left(\frac{y_i - y_{fit,i}}{\sigma_i}\right)^2 \frac{1}{n - n_{par}} \quad [4]$$

In this equation, y_i is an experimental intensity data point, $y_{fit,i}$ is a model intensity point, σ_i is the error on the intensity, n is the number of data points, and n_{par} is the number of fitting parameters. In the case of the cylinder, there are three fitting parameters (A, R, and L), and in the case of the sphere and infinite cylinder, there are two (A and R). Values of χ^2 close to 1 indicate good fits.

The peak fitting was performed first, as this fit was later used to define a start to the fitting range for the form factor fitting. As previously discussed, the peak arises primarily due to the structure factor. However, there is also a contribution due to the form factor in the region near the peak. Following the method used by Yamaguchi et al. (7), we assumed that the form factor follows an approximate q^{-1} dependence in the region near the peak. Assuming that $I(q)$ is given by the product of $F(q)$ and $S(q)$, we divided $I(q)$ by q^{-1} to obtain an estimate for $S(q)$ as $I(q)\times q$. The fit range for the Gaussian approximation was determined by finding the maximum data point in $I(q) \times q$, not including the high intensity at low q which may be due to the direct beam or subtraction artifacts. A range was obtained by taking data points above 90% of this maximum value. The left plot in Figure 1 shows the result of this fit. The weakness of this fit is that it may not accurately capture the shape of the peak; for example, the 10 wt.% ionomer concentration profile shows the fit curve exceeding the extent of the data near the peak. Simply reducing the threshold may not always provide a better fit because as higher q values are included, there is an increased intensity contribution from the form factor, separate from the intensity contributions causing the peak. Therefore, we extended the range to the left only, by half the width of the original interval. The result is shown in the right plot of Figure 1.

For form factor fitting, we sought to select a fitting range for q that excludes the interference peak, which is mostly due to the structure factor. Knowing that the effect of the structure factor is greatly diminished at larger q (6), we expected the fit quality to improve as the fit range includes fewer points in the intermediate q range where the peak is prominent. To observe the effect of the fitting range on fit parameters and fit quality, we performed the fitting repeatedly, sweeping over different starting points for the fitting range. As before, the MATLAB 'fit' function was used, with the Trust-Region algorithm for nonlinear least squares optimization, and using weights equal to the inverse of the

experimental uncertainty of I. To expedite the fitting process, we down-sampled the experimental data by a factor of two, and only evaluated the fit for every other point; that is, every fourth point in the original, non-sampled data. For each fit, we obtained the fit parameters and calculated the reduced χ^2 value.

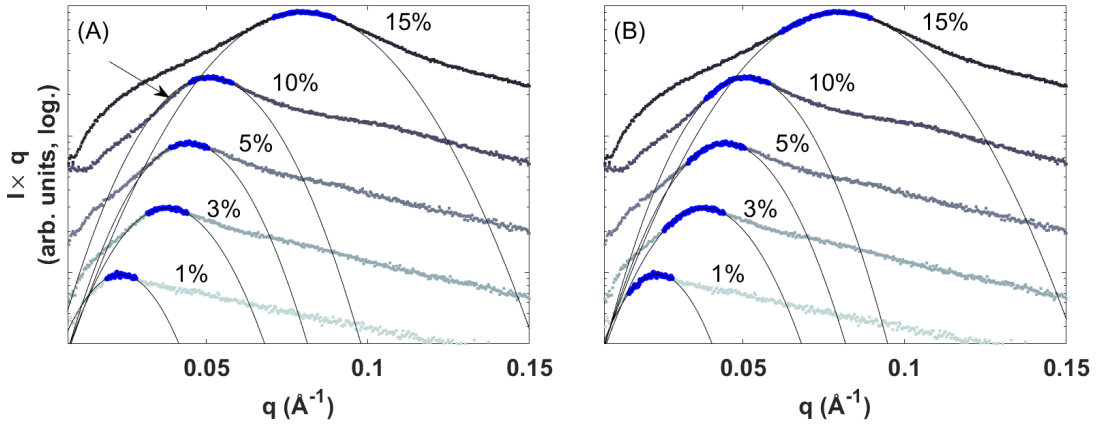

Figure 1: Gaussian peak fitting to approximated structure factors $I(q) \times q$ for ionomer concentrations between 1 wt.% and 15 wt.%. The fitting range is indicated by the larger blue point markers. A symmetric fitting range (A) and a fitting range extended to lower q (B) results in better fits. Profiles have been shifted vertically for clarity.

To report a value for a radius, we selected a specific starting point based on a criterion on the Gaussian fit to the peak. Namely, a parameter N was selected between 0 and 1, and the larger value of q at which the value of the Gaussian was N times the maximum intensity was used as the starting point. Beginning with this fit, we selected ten successive fits with incrementally increasing start points. Any fits that were outliers, defined as having a reduced χ^2 value greater than some threshold, or as having R more than double compared to the previous fit, were not included. The average and standard deviation of R were reported for these ten fits.

Results

The scattering profiles and form factor fits for the three models are shown in Figure 2, with an overlay of each model for a fit range corresponding to $N = 0.3$. As shown by the highlighted regions, the most prominent regions of the peak were excluded from the fitting with this method. For these data, the sphere form factor appears to be a poor model, as the knee-like downturn of the model tends to overshoot the data. In contrast, the two cylinder fits follow the contour of the data more closely. The deviation between the data and the model at high q, around 0.2 Å^{-1}, is present in form factor fits in the literature, and may be due to the effects of the interface between the scattering particle and the solvent (7,9).

The trend in fit quality is shown in Figure 3, assessed using the reduced χ^2 parameter from Eq. [4]. The value of the χ^2 parameter was substantially larger for the sphere fits compared to the cylinder fits. For all three models, the χ^2 value decreased as the fit range start point increased, although the spherical model reached a local minimum and increased again. The trends were smooth, except at high q values for the cylinder models. For the

infinite cylinder, there may have been a second locally optimal solution with orders of magnitude higher χ^2, which the optimizer found for certain choices of start point, as shown by the jumps and short but smooth segments with high χ^2. In the case of the finite cylinder, there seemed to be two or more locally optimal solutions with high χ^2 values, which appeared frequently after about 0.13 Å^{-1}, causing a highly scattered appearance. However, there continued to be solutions following the smooth trend lines extending from lower q, meaning the average R corresponding to the best, low χ^2 fits could still be calculated at higher q start points using an outlier exclusion method.

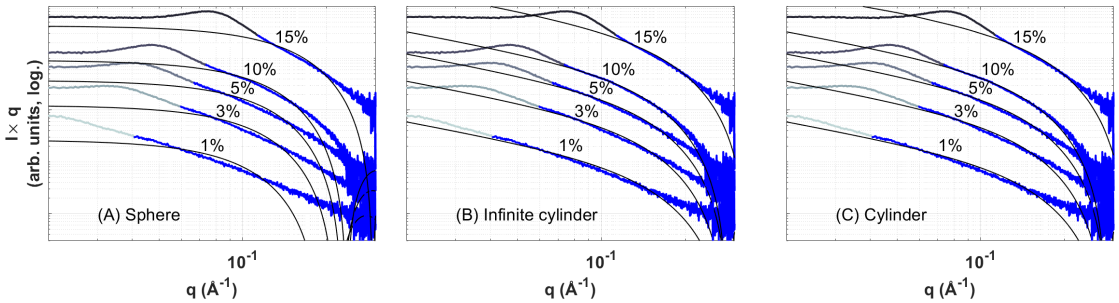

Figure 2: Form factor fitting to $I(q)$ using spherical (A), infinite cylindrical (B), and cylindrical (C) models. The fitting range, highlighted, is defined using a proportion N of the maximum of the earlier Gaussian fits. The N = 0.3 case is shown here. Profiles have been shifted vertically for clarity.

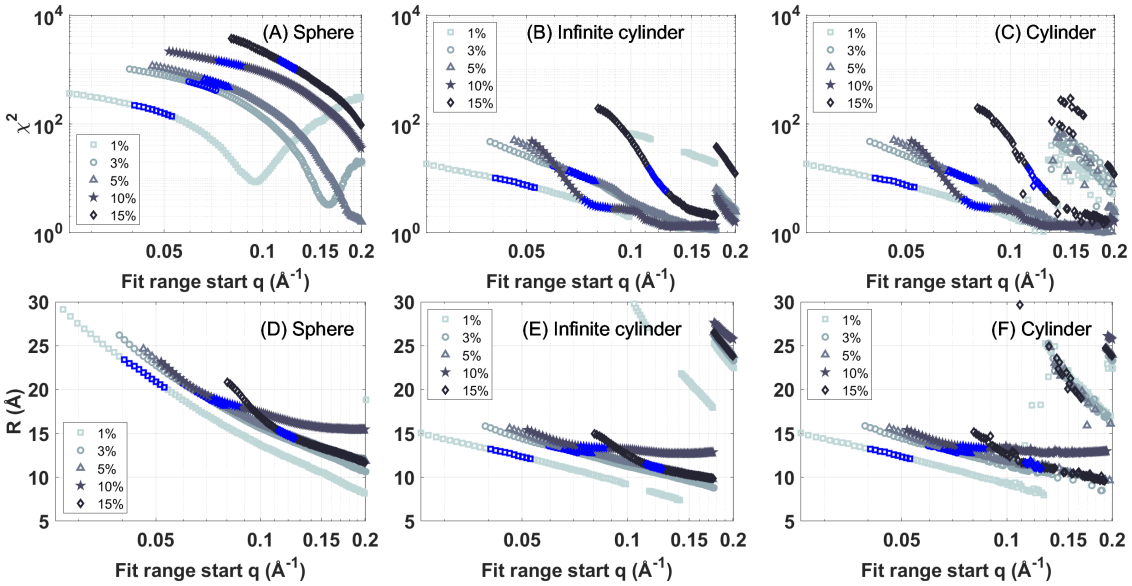

Figure 3: Dependence of the goodness-of-fit parameter χ^2 (A-C) and fit radius R (D-F) on the start of the fitting range. Points used to report averages in the N = 0.3 case are highlighted. In the case of the cylindrical fits at higher q fit range start points, the least squares optimization begins finding solutions with much higher χ^2 and R values, resulting in breaks in the otherwise nearly continuous trends.

Figure 3 also shows the dependence of the fit radius on the start point. For all three models, there was a decreasing trend as the start point increased in q. Notably, the value of R could vary by several angstroms depending on the choice of start point. The locally optimal, high χ^2 solutions could also be seen in the radius fits as discontinuities or scattered points.

Sensitivity

To illustrate the effect of the fitting range, we evaluated a sensitivity parameter as the incremental change in the fit R per change in the fitting range. Figure 4 shows the variation of this parameter with the start point. The magnitude of the sensitivity decreased as the start point increased in q, except at the lowest q values where the interference peak may have had a substantial effect on the fitting. In general, this suggests that the fit R approaches a stable value as the fit range moves to the right; however, this may be because of the reduced number of points in the fit. For instance, for the fit start of 0.2 $Å^{-1}$, only 150 down-sampled points were used.

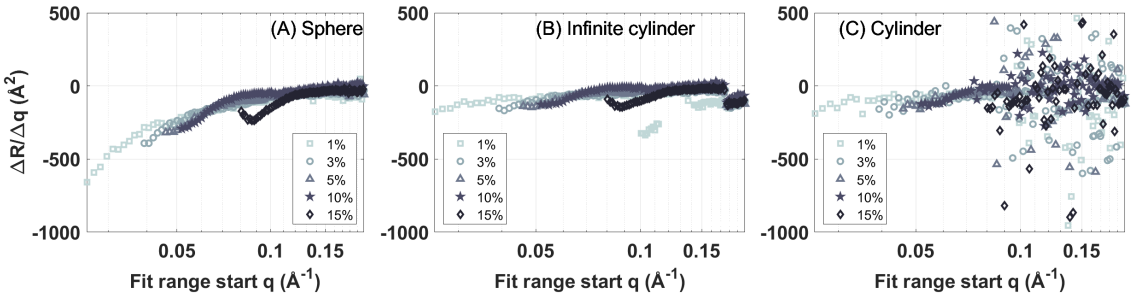

Figure 4: Sensitivity of the fit radius R with respect to the start of the fitting range, expressed as a numerical derivative. The sensitivity generally decreases as the start of the fit range is extended to greater q. In the case of the cylindrical model, the tendency for least squares optimization to find solutions with very different radii at higher fit range starting points causes large fluctuations in the sensitivity.

Trends Over the Concentration Series

To show the effect of the parameter N on the reported value of R, we calculated R using four different values of N between 0.01 and 0.3. Figure 5 shows the effect of this change on the trends over the ionomer concentration series. Although the value of the radius could vary by several angstroms depending on the choice of N, the trend over the ionomer concentration series remained mostly the same. The exception in these data were the relative radii of 3 wt.% and 5 wt.% ionomer using cylindrical fits – from $N = 0.01$ to $N = 30$, the radius for the 5 wt.% sample changed from greater to less than the 3 wt.% sample.

For the sphere fitting, the radius decreased with ionomer concentration from about 18-22 Å at 1 wt.% and 13-15 Å at 15 wt.%. The exception to the trend was the 10 wt.% sample, which had an R nearly the same as or slightly greater than the 5 wt.% sample. The cylinder models had nearly flat trends, with R between 11-14 Å at 1 wt.% to 10 wt.%, and a drop in radius at 15 wt.% to 10-12 Å. Larger values of N, which bring the fit range start point to lower q values, had higher R values.

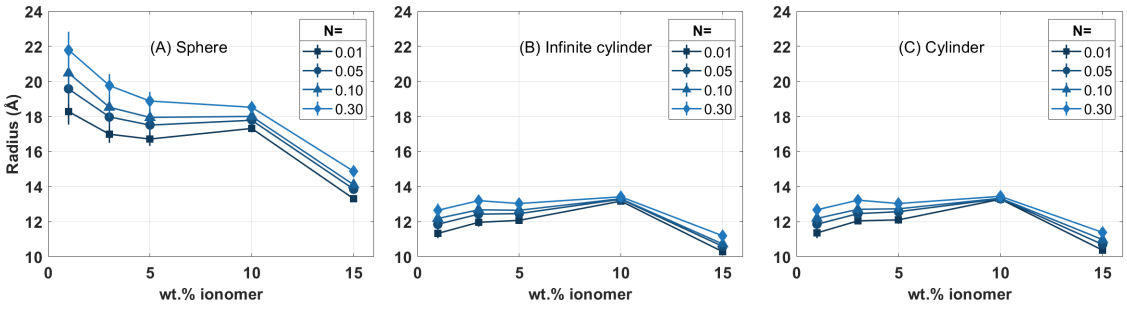

Figure 5: Trends of average radius for ten fits with one standard deviation error bars for the spherical (A), infinite cylindrical (B), and cylindrical (C) models, using values of N between 0.01 and 0.30.

Discussion

The three sets of form factor fit in Figure 2 revealed a higher fit quality for the cylindrical fits compared to the spherical fit, supporting the idea that the aggregates of Nafion™ are more rod-like than spherical. This pattern of better fits for a cylinder model compared to a sphere agrees with the finding by Khandavalli et al., who also tried both models (9). For the two cylinder models, the infinite and finite form factors produce similar results, both in the fit R and in the trends of χ^2 and R with the start point. The similarity suggests that the length scales of the samples are sufficiently long that the differences between the models are small. In other words, for Nafion ™ dispersions, it may be sufficient to use the simpler infinite cylinder fit, which typically solves much faster due to the simpler expression and fewer fitting parameters.

One of the reasons one would prefer the finite cylinder model is to extract the length in addition to the radius. This is challenging because, for a cylindrical scatterer, information about the cylinder length comes from the low-q region (10). Yamaguchi et al. observed that the interference peak obscures this region (7), and Gupit et al. observed that even in the case of low concentration for which the peak is not strong, they could not fit for the length (8). Their fitting suggested a cylindrical length over 350 Å, which is greater than the $1/q$ limit for their instrument range (8). Therefore, the infinite cylinder model can be a good alternative to the popular cylinder model if the aggregates are sufficiently long. Another difference we discovered is the tendency of the least squares solver to find locally optimal solutions with poor χ^2 values compared to neighboring fits. This tendency may be attributable to the choice of parameters in the least squares solver, such as the initial guesses, which can be adjusted if the fits in that q-region are of interest. However, limiting the fitting range to these high-q values, often quite far from the end of the interference peak, can mean data from the intermediate-q region, which contains cylinder radius information, are excluded (10).

The values of radius obtained by the cylinder fitting are similar to those reported in prior studies of Nafion in water-propanol solutions. Xu et al. reported a radius of 15 Å at a 5 wt.% concentration of Nafion™, corroborated by TEM imaging (1). Yamaguchi et al. found a radius of 9 to 14 Å for a range of ratios of water to 1-propanol encompassing that used in the present work, at a concentration of 30 g/dm^3 (7), which corresponds to roughly

3 wt.%, assuming the density of the dispersion is close to that of water. Our measurements, between 11-14 Å at comparable concentrations, show that the cylinder model is relatively robust to the choice of fitting range start point, within a 1.3 Å or 12% difference between $N = 0.01$ and $N = 0.3$ for the 1 wt.% sample. The sensitivity of the cylindrical fits is low for the fit ranges corresponding to $N = 0.3$ or less, with a sensitivity less than 100 $Å^2$, or 1 Å per 0.01 $Å^{-1}$ change in the fit range, further supporting the robustness of the model.

Conclusions

By fitting spherical and cylindrical form factors to data obtained from a series of Nafion™ D2020 ionomer dispersions, we have demonstrated the importance of the fitting range when determining fit parameters. In the case of the commonly used cylinder model, selecting a different fitting range can change the fit radius by multiple angstroms, which can affect trends in experiments investigating the effects of small changes to dispersion properties. Therefore, we argue that it is important to establish a consistent method of selecting a fitting range for all samples. In this work, we presented one technique involving fitting a Gaussian function to the interference peak and taking a threshold of the fit at some proportion N of the maximum. However, if it is feasible to calculate a sweep of fits with varied fitting ranges, it could be reasonable to establish some criteria related to the fit-range dependence; for example, selecting a threshold based on the fit sensitivity or the goodness-of-fit parameter.

In comparing the three models, we have found consistent results with the literature that suggest ionomer aggregates will be cylindrical with the solvents and ionomer concentrations investigated. Given that the cylindrical shape is appropriate, we further suggest that the infinite cylinder model may be the preferable choice for fitting due to the close agreement with the finite cylinder model at a reduced computational due to not needing to evaluate the integral. Additionally, the reduced number of fitting parameters could lead to reduced fluctuation in fit results with minor changes in the choice of fit range, as was seen for the finite cylinder model. In future work, we plan to apply the fitting techniques described in this report to SAXS data of new ionomer materials previously investigated for their ability to enhance PEMFC performance.

Acknowledgments

The authors acknowledge use of the Materials Characterization Facility at Carnegie Mellon University supported by grant MCF-677785. Funding for the SAXS/WAXS instrumentation used in this research was provided by the NSF Major Research Instrumentation (MRI) award number CMMI-2117523. Eugene Jeong was supported by the Department of Defense (DoD) through the National Defense Science & Engineering Graduate (NDSEG) Fellowship Program.

References

1. F. Xu, H. Zhang, J. Ilavsky, L. Stanciu, D. Ho, M. J. Justice, H. I. Petrache, and J. Xie, *Langmuir*, **26**, 19199 (2010).

2. J. P. Braaten, N. N. Kariuki, D. J. Myers, S. Blackburn, G. Brown, A. Park, and S. Litster, *J. Power Sources*., **522**, 230821 (2022).
3. J. Marcinkoski, R. Vijayagopal, J. Adams, B. James, J. Kopasz, and R. Ahluwalia, *DOE Advanced Truck Technologies. Subsection of the Electrified Powertrain Roadmap – Technical Targets for Hydrogen-Fueled Long-Haul Tractor-Trailer Trucks* https://www.hydrogen.energy.gov/docs/hydrogenprogramlibraries/pdfs/19006_hydrogen_class8_long_haul_truck_targets.pdf?Status=Master (2019).
4. L. Rubatat, G. Gebel, and O. Diat, *Macromolecules*, **37**, 7772 (2004).
5. P. Aldebert, B. Dreyfus, and M. Pineri, *Macromolecules*, **19**, 2651 (1986).
6. B. Loppinet and G. Gebel, *Langmuir*, **14**, 1977 (1998).
7. M. Yamaguchi, T. Matsunaga, K. Amemiya, A. Ohira, N. Hasegawa, K. Shinohara, M. Ando, and T. Yoshida, *J. Phys. Chem. B*, **118**, 14922 (2014).
8. C. I. Gupit, X. Li, R. Maekawa, N. Hasegawa, H. Iwase, S. Takata, and M. Shibayama, *Macromolecules*, **53**, 1464 (2020).
9. S. Khandavalli, J. H. Park, H. H. Winter, D. J. Myers, M. Ulsh, and S. A. Mauger, *Macromolecules*, **56**, 6988 (2023).
10. B. Hammouda, *J. Appl. Cryst.*, **43**, 716 (2010).
11. C. Welch, A. Labouriau, R. Hjelm, B. Orler, C. Johnston, and Y. S. Kim. *ACS Macro Lett.*, **1**, 1403 (2012).
12. A. Tarokh, K. Karan, and S. Ponnurangam, *Macromolecules*, **53**, 288 (2019).
13. T. Mabuchi, S. F. Huang, and T. Tokumasu, *Macromolecules*, **53**, 3273 (2020).
14. J. B. Hopkins, *J. Appl. Cryst.*, **57**, 194 (2024).
15. G. Fournet, *B. Mineral.*, **74**, 37 (1951).
16. G. Porod, in *Small Angle X-Ray Scattering*, O. Glatter and O. Kratky, Editors, p. 32, Academic Press, London (1982).
17. M. Doucet, J. H. Cho, G. Alina, Z. Attala, J. Bakker, P. Beaucage, W. Bouwman, R. Bourne, P. Butler, I. Cadwallader-Jones, K. Campbell, T. Cooper-Benun, C. Durniak, L. Forster, P. Gilbert, M. Gonzales, R. Heenan, A. Jackson, S. King, P. Kienzle, J. Krzywon, B. Maranville, N. Martinez, R. Murphy, T. Nielsen, L. O'Driscoll, W. Potrzebowski, S. Prescott, R. F. Leal, P. Rozyczko, T. Snow, A. Washington, L. Wilkins, and C. Wolf. *SasView version 5.0.3* http://www.sasview.org/ (2023).